International Journal of Plasticity 120 (2019) 340–360

Contents lists available at ScienceDirect

International Journal of Plasticity

journal homepage: www.elsevier.com/locate/ijplas

Material response, localization, and failure of an aluminum alloy under combined shear and tension: Part I experiments

Martin Scales, Kelin Chen, Stelios Kyriakides*

Research Center for Mechanics of Solids, Structures & Materials, ASE, The University of Texas at Austin, Austin, TX 78712, USA

ARTICLE INFO

Keywords:
Ductile failure
Combined shear and tension
Low triaxiality
Failure strain vs. triaxiality

ABSTRACT

This two-part series of papers presents complementary experiments and analyses of ductile failure of an aluminum alloy in the challenging regime of moderate to low stress triaxiality. Part I uses a custom tension-torsion experimental setup to establish the response and the onset of failure under proportional and non-proportional stress histories that form the basis for the numerical simulations in Part II. The test section of the adopted tubular specimen allows large localized strains to develop unimpeded, which were captured using high-resolution digital image correlation (DIC). The measured failure strains exhibit a monotonic decrease as triaxiality increases, similar to the results of Scales et al. (2016). A difference is that the present failure strains are calculated by integrating the work-compatible equivalent plastic strain increments over the loading history, which necessitates the use of a constitutive model. It is shown that for triaxialities greater than 0.2 the integrated failure strains are very close to the values measured directly from the last DIC image. Furthermore, the choice of constitutive model does not significantly affect the measured strains. For the four corner-path experiments, the state of stress and equivalent strain at failure were found to be close to the values of the corresponding radial paths.

Microscopic evaluations indicated that the material exhibited limited void growth until just prior to rupture. Part II of this series investigates the extent to which properly-calibrated plasticity models can reproduce the high strains in the localized zones.

1. Introduction

Ductile failure is a major factor in the end of life of structures under extreme loadings such as aircraft, naval vessels, nuclear reactor containment vessels, pipelines, vehicle crushing, civil structures under seismic loadings, and others. The commonly used Johnson-Cook (1985) failure criterion assumes that the strain at failure is governed by stress triaxiality as suggested in McClintock (1968, 1971), Rice and Tracy (1969), Gurson (1977), Tvergaard (1990), Benzerga and Leblond (2010), etc. More recently dependence on the third invariant of the deviatoric stress tensor has been suggested (e.g., Bao and Wierzbicki (2004); Bai and Wierzbicki (2008, 2010); Barsoum and Faleskog (2007)). In support of this notion, experiments on aluminum alloys involving shear-dominant stress states reported failure strains that decreased as triaxiality decreases, developing a local minimum near triaxiality of zero (see also Beese et al. (2010)). Collectively these results generated renewed interest in ductile failure and spawned a significant number of mostly analytical studies and a select number of more careful experimental investigations. The analytical studies not withstanding, experiments such as those of Faleskog and Barsoum (2013), Haltom et al. (2013), Ghahremaninezhad and Ravi-Chandar (2012, 2013), Papasidero et al. (2015), Scales et al. (2016), Abi-Akl and Mohr (2017), and Ha et al. (2018) reported monotonic decreases in

* Corresponding author.
E-mail address: skk@mail.utexas.edu (S. Kyriakides).

https://doi.org/10.1016/j.ijplas.2019.04.004
Received 12 January 2019; Received in revised form 14 March 2019; Accepted 4 April 2019
Available online 15 April 2019
0749-6419/

failure strain with triaxiality, thus challenging some of the claims to the contrary mentioned above.

This rather murky state of affairs is partly caused by practical challenges encountered in the testing of materials, especially in sheet metal form under combined shear and axial loads. Most experimental setups are characterized by non-uniform 3-D stress and strain fields, which are extracted numerically using an assumed, and in some cases inappropriate, constitutive model. Moreover, many specimen geometries used constrain the development of localization that precedes failure.

In our previous work on ductile failure of Al-alloys under low to moderate triaxiality values (Haltom et al. (2013); Scales et al. (2016)), some of these challenges were overcome by generating strain-triaxiality failure loci through tension-torsion experiments on two-inch (51 mm) diameter tubes. The test specimens had a 0.62 in (15.8 mm) long and 0.038 in (0.966 mm) thick test section, which is free of the stress-concentrations that develop at the free ends of other test set-ups. Simultaneously, its length allows the ensuing localization to develop free of constraints. High-resolution stereo digital image correlation (DIC) enabled direct measurement of the deformation in the test section, including in the narrow zone of localization, to values significantly higher than previously reported. Furthermore, parallel studies revealed that the highly deformed material remained essentially free of damage until very close to rupture.

In the present pair of sister papers the subject is revisited; a new set of proportional and non-proportional nominal stress experiments are performed and reported in Part I. The experiments are simulated numerically in Part II using suitably calibrated constitutive models. The aim is first to establish how far plasticity alone can go in predicting the high strains that develop in the localized zone, and second demonstrate the effect of the yield function adopted on the results. The work includes calibration of an anisotropic yield function, establishment of the material hardening from a simple shear test and supporting experiments, and investigation of the effect of yield function on the measured failure strains.

2. Experimental

2.1. Material and test set-up

The material tested is Al-6061-T6 provided by Kaiser Aluminum in the form of 2.0 × 0.188 in (51 × 4.78 mm) extruded tubular stock. The alloy composition and grain morphology are given in Appendix A. Using as reference the inner diameter, a 0.60 in (230 mm) long test section was machined in the middle of a 9 in (230 mm) long specimen resulting in a 0.400 in (10.2 mm) straight section with 0.039 in (0.990 mm) wall (Fig. 1; exact wall thickness of each specimen given in Table 1).

The experiments were performed in an axial-torsional testing machine following the same procedure as in Scales et al. (2016). Steel plugs are inserted into the specimen end sections and the specimen is loaded into the test set up shown in Fig. 2. The specimen is gripped on the top and bottom by pressurized clamps (ETP-TECHNO), which enable nearly-axisymmetric gripping and maintain the axial alignment that is critical to these experiments. For the main body of the experiments, the specimens were loaded along radial paths in the nominal axial-shear stress space:

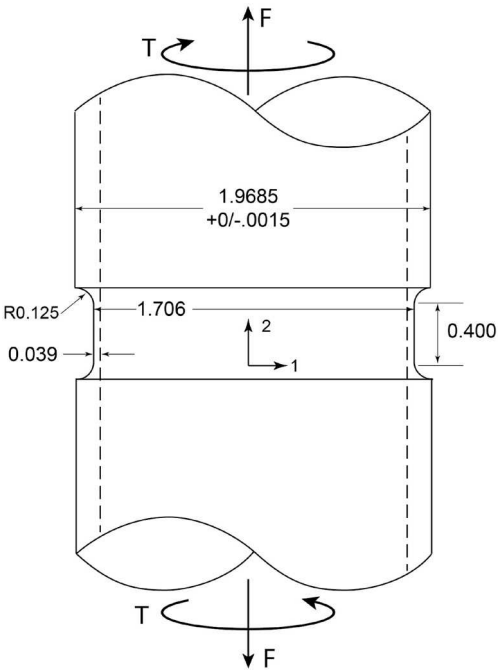

Fig. 1. Schematic of the tubular test specimen used in the tension-torsion experiments (1 in = 25.4 mm).

Table 1
Main parameters for tension-torsion radial and corner stress path experiments and the stresses and strains at the load maxima.

Exp. No.	Tube No.	α	R in (mm)	t_o in (mm)	Ξ_o%	$\Sigma_{\max}$ ksi (MPa)	$\mathscr{T}_{\max}$ ksi (MPa)	ε_{22L}	ε_{12L}
11	3	0	0.837 (21.3)	0.0461 (1.17)	3.9	0	–	0	–
4	1	0.49	0.833 (21.2)	0.0392 (1.00)	4.2	13.0 (89.7)	26.2 (181)	0.060	0.451
10	3	0.75	0.834 (21.2)	0.0392 (1.000)	5.4	19.1 (132)	25.3 (174)	0.079	0.360
2	1	1.0	0.834 (21.2)	0.0386 (0.098)	3.6	24.4 (168)	24.1 (166)	0.067	0.209
1	1	1.5	0.834 (21.2)	0.0394 (1.00)	5.1	31.9 (220)	21.4 (147)	0.058	0.100
3	1	1.99	0.834 (21.2)	0.0390 (0.99)	4.8	36.5 (252)	18.2 (126)	0.077	0.081
5	1	3.0	0.834 (21.2)	0.0387 (0.98)	3.1	41.6 (287)	13.5 (93.1)	0.075	0.041
7	1	4.16	0.833 (21.2)	0.0388 (0.99)	3.5	43.4 (300)	10.4 (71.7)	0.084	0.036
9	2	PS	0.833 (21.2)	0.0389 (0.99)	5.8	46.9 (323)	0	0.106	0
14	3	2.0 ($\Sigma \rightarrow \mathscr{T}$)	0.834 (21.2)	0.0390 (0.99)	5.2	32.0 (221)	21.0 (145)	0.070	0.097
17	2	2.0 ($\mathscr{T} \rightarrow \Sigma$)	0.834 (21.2)	0.0388 (0.99)	3.0	39.9 (275)	16.0 (110)	0.096	0.070
12	3	1.0 ($\Sigma \rightarrow \mathscr{T}$)	0.833 (21.2)	0.0390 (0.99)	4.8	23.1 (159)	23.9 (165)	0.074	0.224
13	3	1.0 ($\mathscr{T} \rightarrow \Sigma$)	0.834 (21.2)	0.0389 (0.99)	4.2	29.8 (205)	22.8 (157)	0.060	0.167

$\Xi_o = \frac{t_{\max} - t_{\min}}{t_{\max} + t_{\min}}$

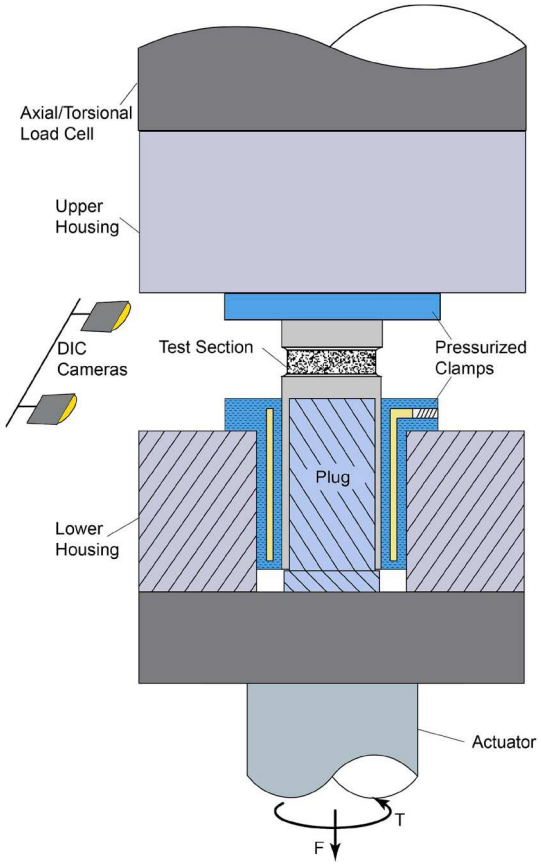

Fig. 2. Illustration of test setup and hardware.

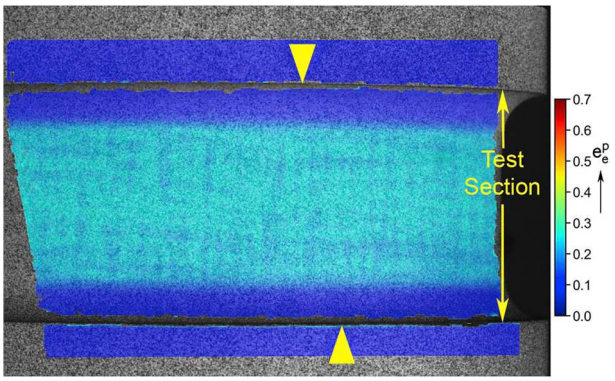

Fig. 3. Example of the region of the specimen surface monitored by DIC. This image is from early in the test when the deformation in the test section is still uniform.

$$\Sigma = \alpha \mathscr{T} \quad \alpha = \text{const.} > 0 \tag{1}$$

(Σ and $\mathscr{T}$ are respectively the nominal axial and shear stresses in the test section). For $\alpha < 3.5$, the machine is operated in rotation and axial load control, with the torque acting as the command signal for the force. The rotation rate is specified to achieve a nominal shear strain rate of roughly $\dot{\gamma} \approx 2 \times 10^{-4}\ \mathrm{s}^{-1}$. For $\alpha \geq 3.5$ the machine is operated in axial displacement and torque control, with the force acting as the command signal for the torque. Four corner paths performed will be described separately.

3D Digital Image Correlation (DIC) is again used to continuously monitor the deformation in the test section during the tests. Our system has two 5 MP digital cameras, each equipped with 50 mm lenses. The smallest possible aperture setting was used to maximize depth of field, and the shutter time was limited to 30 ms by the use of external lighting. Image acquisition and processing was done via GOM ARAMIS v6.3. The computed area includes the entire length of the test section, an additional 0.2 in (5 mm) above and below the test section, and spans approximately 110° circumferentially. The image in Fig. 3 shows the monitored are uniformly deformed. Images were acquired at a frame rate of 12 per minute up to the limit load, and at 30 frames per minute subsequently.

2.2. Stresses

Let $\{\sigma_{ij}, s_{ij}\}$ be the Cauchy stress components and their deviatoric counter parts, and $\{\sigma_i, s_i\}$ be the corresponding principal values. Assume that in the test section the through thickness stresses are negligibly small. Furthermore, for the purpose of estimating the stress and strain state at failure assume that its radius remains unchanged. Then the non-zero stresses are:

$$\sigma_{22} = \sigma,\ \sigma_{12} = \tau,\ \sigma_{11} = \beta\sigma, \tag{2a}$$

(where "1" is in the hoop and "2" in the axial direction—see also Fig. 1). The principal stresses are

$$\sigma_{1,2} = \frac{\sigma(1+\beta)}{2} \pm \sqrt{\sigma^2\left(\frac{1-\beta}{2}\right)^2 + \tau^2}. \tag{2b}$$

The mean stress is then:

$$\sigma_m = \sigma(1+\beta)/3 \tag{3}$$

For non-quadratic incompressible plasticity the equivalent stress is given by (Hosford (1972)):

$$\sigma_e = \left\{\frac{1}{2}\left[\left(\sigma_1 - \sigma_2\right)^k + \sigma_1^k + \sigma_2^k\right]\right\}^{1/k}. \tag{4}$$

For example, for von Mises

$$k = 2, \beta = 1/2, \sigma_m = \sigma/2, \text{ and } \sigma_e = \sqrt{\frac{3}{4}(\sigma^2 + \tau)} \tag{5}$$

In this study $k = 8$ was adopted in (4)–Hosford yield function (H8)— for which β depends on the biaxiality ratio α. The third invariant of the deviatoric stress is

$$J_3 = s_1 s_2 s_3 = (\sigma_1 - \sigma_m)(\sigma_2 - \sigma_m)(\sigma_3 - \sigma_m). \tag{6}$$

The Haigh-Westergaard variable θ is given by:

$$\cos 3\theta = \left(\frac{3\sqrt{3}}{2}\frac{J_3}{J_2^{3/2}}\right), \tag{7}$$

and

$$\bar{\theta} = 1 - 6\theta/\pi \text{ (after Wierzbicki and co} - \text{workers)}, \tag{8}$$

and finally, the Lode parameter

$$\mu = \frac{2\sigma_2 - \sigma_1 - \sigma_3}{\sigma_1 - \sigma_3}, \ \sigma_1 > \sigma_2 > \sigma_3, \tag{9}$$

2.3. Calculation of strain using DIC

ARAMIS software version 6.3 was used to perform the digital image correlation. We analyzed experiment images using the recommended subset size of 19 × 19 pixels (corresponding to roughly one-third of the specimen initial wall-thickness, t_o), and a subset spacing of 6 pixels ($\approx t_o/10$) to ensure resolution of the anticipated deformations. ARAMIS discretizes the surface of the specimen into a uniform grid of points, with each point located at the center of a facet in the reference image. The displacement of each of these points is then calculated by tracking the facet through subsequent images via the correlation algorithm. Finally, ARAMIS calculates the in-plane deformation gradient tensor $\boldsymbol{F}$ at each of these discrete points by considering the displacement of each point and its neighbors, and numerically differentiating the local displacement field.

In Scales et al. (2016), we computed the stretch tensor $\boldsymbol{U} = (\boldsymbol{F}^T\boldsymbol{F})^{1/2}$ via polar decomposition of $\boldsymbol{F}$, and then calculated the principal stretches λ_α, $\alpha = 1,2$ and corresponding principal logarithmic strains $e_\alpha = \ln\lambda_\alpha$. From there, we invoked incompressibility and neglected elastic deformations to calculate the total von Mises equivalent plastic strain. Barsoum and Faleskog (2007) and Faleskog and Barsoum (2013) showed the conventional integration of the incremental measure of strain to be more accurate for shear dominant stress paths. Thus in the present work the incremental equivalent plastic strain is integrated over the path. The difference between the two schemes will be quantified in Section 4. The following scheme accounts for the large rotation of the material frame that occurs in these experiments.

The work conjugate strain increment to the Cauchy stress at a point is computed from:

$$d\boldsymbol{\varepsilon} = sym(d\boldsymbol{F}\boldsymbol{F}^{-1}), \tag{10}$$

where $d\boldsymbol{F}$ for stage n is approximated discretely as $d\boldsymbol{F} \approx (\boldsymbol{F}_n - \boldsymbol{F}_{n-1})$. Then the work-compatible equivalent plastic strain *increment* is computed using the equivalent stress of the adopted constitutive model

$$de_e^p|_n = \frac{\sigma_{ij}d\varepsilon_{ij}}{\sigma_e} = \frac{\sigma_{11}d\varepsilon_{11} + \sigma_{22}d\varepsilon_{22} + 2\sigma_{12}d\varepsilon_{12}}{\sigma_e}, \tag{11}$$

where the elastic components of the strain increments are again neglected. Finally, this is integrated from the reference to the current stage, N,

$$e_e^p = \int_n de_e^p|_n \approx \sum_{n=1}^{N} de_e^p|_n. \tag{12}$$

The individual strain components can be summed in a similar fashion to generate the complete strain history. This calculation method was found to be somewhat sensitive to the noise inherent in DIC data, and a rigorous filtering scheme was developed to ensure erroneous data was not introduced into the calculation:

- Only points that exist in every stage are considered.
- Point columns are scanned, and the location of the maximum equivalent strain in each column is identified.
- Columns that are missing points within two-thirds of the initial wall-thickness above and below the maximum points are rejected.
- Column maxima that do not have all eight neighbors are rejected.

These criteria readily facilitate the calculation of strains incrementally and remove most of the points from consideration which could be prone to error. A final filtering step is employed in which points whose strain is seen to “grow too quickly” are rejected from further consideration, as these are judged to most likely be non-physical deformations stemming from the software's difficulty with correlating in the zones of large and highly-local deformations. These criteria together resulted in reliable data with a large enough number of points for statistically-meaningful analysis. Data presented as *Mean* values are calculated as the average of the column maxima following this filtering, while the *Max* data are taken from the single point with the maximum equivalent plastic strain in the final stage prior to failure.

3. Tension torsion results

3.1. A representative experiment

The results of a representative experiment in which $\alpha = 0.75$ are presented in detail. Table 1 lists under Exp. No. 10 the mean R and average wall thickness t_o of the test section, as well as its eccentricity measured through: $\Xi_o = (t_{o\,\max} - t_{o\,\min})/(t_{o\,\max} + t_{o\,\min})$. To

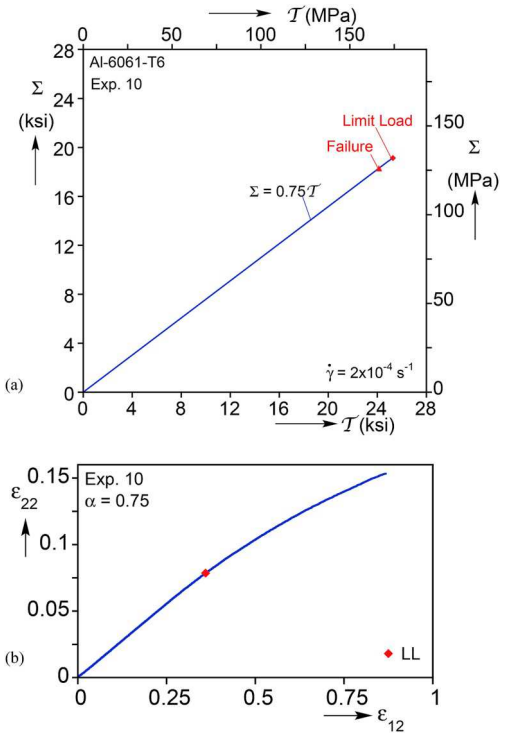

Fig. 4. (a) Nominal axial-shear stress history for $\alpha = 0.75$. The limit load is marked by ◆ and failure by ▲. (b) Measured *Mean* strain history for the same experiment.

ensure that failure initiated within the DIC field of view, the specimen is oriented with the slightly thinner side facing the cameras. Fig. 4a shows the nominal shear-axial stress ($\Sigma - \mathcal{T}$) radial path traced, and Fig. 5a and b the shear stress-rotation ($\mathcal{T}$–ϕ) and axial stress-elongation ($\Sigma - \delta/L_g$) responses respectively. Rotation and elongation are established via DIC measurements from just outside the test section, and form a gage length $L_g = 0.65$ in (16.5 mm). The responses in Fig. 5 exhibit a linear region followed by plastic deformation and mild hardening. At a rotation of 13.4° and normalized elongation of 0.038, the responses reach a load maximum (or limit load) indicated in the responses with a caret "^", and at the end of the radial path in Fig. 4a with ◆. The values of the nominal stresses at this point are listed in Table 1 under ($\Sigma_{\max}$, $\mathcal{T}_{\max}$) and the corresponding strains under (ε_{22L}, ε_{12L}). Beyond the maxima, deformation begins to localize and the two loads decrease with the rate of load drop accelerating up to the onset of failure (marked in Fig. 4a with ▲). Failure in this experiment was accompanied by a sudden drop in the loads drawn with dashed lines in the two responses. About one-third of the circumference ruptured, including part of the section monitored with DIC, but the specimen remained intact thus enabling subsequent evaluation of the facture surface.

The *Mean* measures of shear (ε_{12}) and axial (ε_{22}) strain are plotted in Fig. 4b, as this was found to be the most consistent measure for the whole set of experiments. The resultant trajectory is nearly linear with a significant portion of the growth coming after the limit load. We note that whereas in the present work the strain components are computed in the reference frame, the values reported in Scales et al. (2016) were calculated in the DIC software's local coordinate systems, which rotate with the material deformation. Consequently the corresponding strain plot in Fig. 9 of that work was nonlinear.

An impression of the localized deformation that develops following the limit load can be obtained from Fig. 6, which shows the last DIC image recorded just before rupture with the computed strain field superimposed on the surface. Deformation is seen to have concentrated in a narrow band in the center of the test section that covers the complete circumference of the tube. The band is not perfectly straight as it tends to adapt to local variations in the microstructure and small geometric imperfections.

A first illustration of the evolution of localization of deformation is shown in Fig. 7a, which plots the equivalent plastic strain vs. the rotation angle ϕ: (i) at the location where the final maximum value was recorded—*Max*; (ii) the *Mean* strain from all maxima in the zone monitored; and (iii) from a site outside the localization zone, *Site B*, identified in the DIC image in Fig. 6. The three strain measures increase at similar rate up to $\phi \approx 8°$. As the limit load is approached (marked with a dashed line), the growth of the *Mean* and *Max* strains gradually accelerates while the rate of growth of the strain at Site B decreases. Beyond the limit load the *Max* and *Mean* strains undergo exponential growth with rotation while the strain at Site B remains essentially unchanged. The *Max* trajectory is consistently higher than that of the *Mean* with the values at the onset of failure being 1.15 and 1.0 respectively.

The spatial evolution of deformation across the localization zone at the site of the *Max* strain is illustrated in Fig. 7b. Plotted is a set of equivalent plastic strain profiles, each $6t_o$ long, at the ten stations marked on the responses in Fig. 5. In stations ① and ② prior to the limit load, the profiles are flat indicating that deformation is uniform across the test section. At the limit load (station ③), a clear concentration of deformation is observed in a zone $2t_o$ wide in the center, across which the average value of strain is 0.4. Beyond the

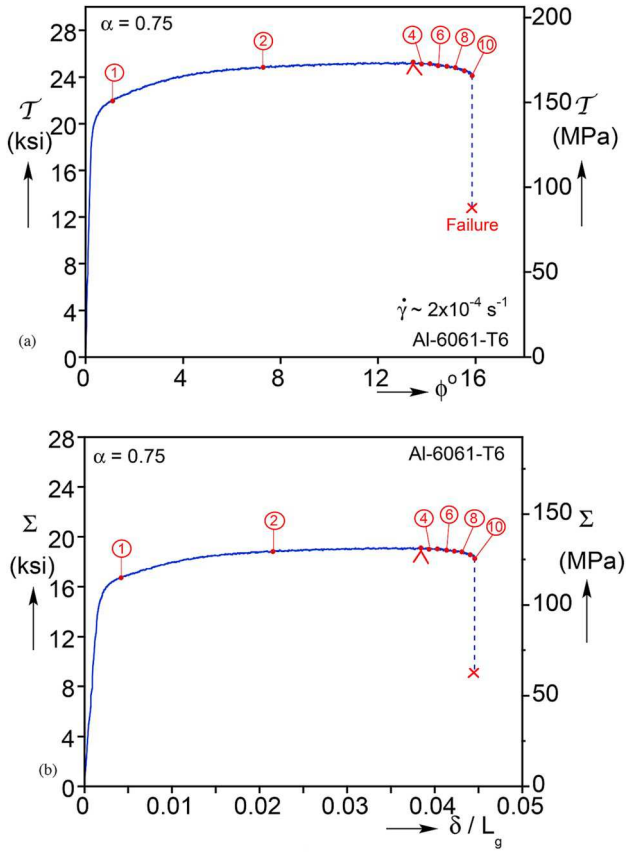

Fig. 5. (a) Nominal shear stress-rotation response for $\alpha = 0.75$. (b) Nominal axial stress-normalized elongation response. Limit load marked by "^" in both.

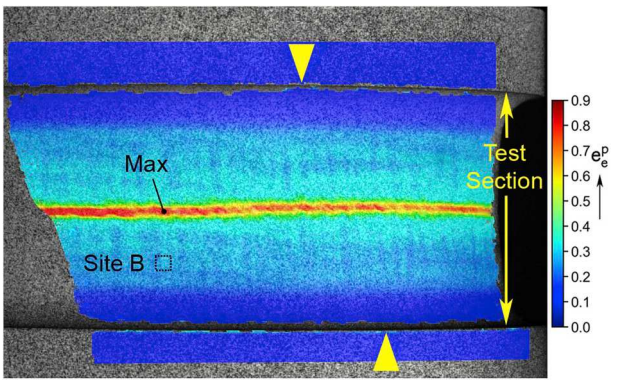

Fig. 6. Equivalent strain measured by DIC overlayed on the specimen surface for $\alpha = 0.75$. This picture is from the last image taken prior to failure.

limit load (stations ④-⑩), deformation concentrates in an increasingly narrower zone about $(1 - 1.5)t_o$ wide, while outside this zone the deformation remains unchanged (as in Site B in Fig. 7a). In image ⑩ just prior to failure, the strain profile reaches a maximum value of 1.15. Remarkably, the strain drops to a value of 0.55 just one-half of a wall thickness in either direction. Achieving such a large gradient in deformation is a testament to the specimen design, which features a uniform test section that is an order of magnitude longer than the wall thickness. The results also highlight the need for a strain measurement technique with resolution that is high enough to capture the deformation in such localized zones such as the 3D DIC method used. The nominal and true stresses at failure are listed in Table 2 under $(\Sigma_f, \mathcal{T}_f)$ and $(\sigma_{22f}, \sigma_{12f})$ respectively where the true stresses are evaluated from the measured force (F) and torque (T) as follows:

$$\sigma_{22} = \frac{F}{2\pi R t_o}\frac{1}{\lambda_3} \text{ and } \sigma_{12} = \frac{T}{2\pi R^2 t_o}\frac{1}{\lambda_3}, \quad \lambda_3 = \frac{t}{t_o}. \tag{13}$$

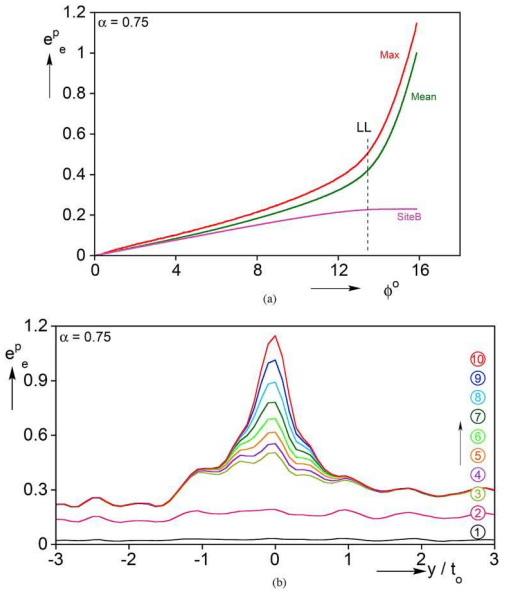

Fig. 7. (a) Measured *Max* and *Mean* equivalent plastic strain in the localizing zone vs. rotation for $\alpha = 0.75$, as well as the average strain from a region outside the localizing zone (*Site B*). The limit load is marked with a dashed line. (b) Equivalent plastic strain profiles across the location of the maximum strain measured prior to failure. The numbers correspond to those indicated in Fig. 5.

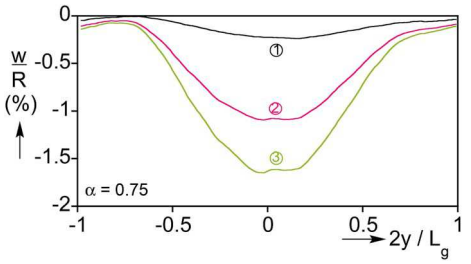

Fig. 8. Radial displacement profiles across the entire length of the test section for $\alpha = 0.75$, at the first three stations marked in Fig. 5.

where t is the current minimum wall thickness of the test section. Also listed is the triaxiality (σ_{mf}/σ_{ef}) based on von Mises and assuming $\sigma_{11f} = \sigma_{22f}/2$. The *Mean* and *Max* measures of equivalent plastic strain are listed under $\bar{e}^p_{ef}$ and e^p_{ef} (these are integrated as in Eq. (12) by assuming $d\varepsilon_{11}$ is negligibly small). Included in Table 2 are the Lode parameters $\bar{\theta}_f$ and μ_f at failure (see Eqs. (8) and (9); note that order of the principal stresses in Eq. (2b) changes for shear dominant stress paths, and this needs to be accounted for in the calculation of μ_f).

The main objectives of the test specimen design in Fig. 1 was to enable the localization to develop free of constraint, and for the through thickness stress to be negligibly small, both of which were achieved. A drawback is that the long thin-walled test section permits a small amount of radial deformation to develop. This is illustrated in Fig. 8, which plots the present experiment the radial displacement, w, across the test section normalized by the mean radius of the test section R. Included are profiles for stations ① through ③. The profiles appear parabolic in shape with the maximum contraction reaching about 1% at station ② and 1.5% at the limit load. Although rather small, this shows that some hoop strain develops in the test section, the effect of which will be further discussed in Part II.

3.2. Summary of tension-torsion results

The results of the whole set of tension-torsion experiments performed are now presented together. They include seven tension-torsion tests with stress ratios $0.5 \leq \alpha \leq 4.0$, an experiment pulled to failure under pure tension (plane strain—PS) and a pure torsion test. The geometry of the test section and the stresses and strains at the limit load are presented in Table 1 while the stress and strain at failure are listed in Table 2. Fig. 9a shows plots of the recorded nominal stress paths and Fig. 10a and b the corresponding nominal shear stress-rotation and axial stress-elongation responses. Fig. 9b shows the *Mean* measures of shear-axial strain measured in the zone monitored using DIC. The *Mean* equivalent plastic strain is plotted in Fig. 11 against the test section rotation.

The results exhibit similar features as those described for $\alpha = 0.75$, and broadly resemble those in Scales et al. (2016). The responses in Fig. 9a show the shear stress and rotation decreasing as α increases while in Fig. 9b the axial stress and elongation

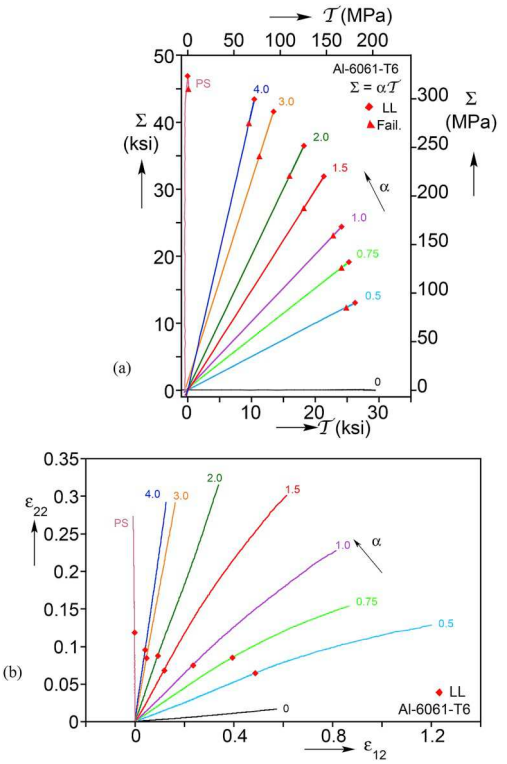

Fig. 9. (a) Nominal axial-shear stress paths for the full set of radial path experiments. The limit loads are marked by ◆ and failure by ▲. (b) Corresponding *Mean* strain paths.

Table 2
Stress and deformation variables at failure.

Exp. No.	α	Σ_f ksi (MPa)	$\mathcal{T}_f$ksi (MPa)	σ_{22f} ksi (MPa)	σ_{12f} ksi (MPa)	$\frac{\sigma_{mf}}{\sigma_{ef}}$	$\tilde{\theta}_f$	μ_f	$\tilde{e}^p_{ef}$	e^p_{ef}
11[a]	0	0	29.4 (203)	0	29.7 (205)	0	0	0	–	–
4	0.49	12.3 (84.8)	24.9 (172)	13.6 (93.8)	27.4 (189)	0.139	0.401	−0.369	1.382	1.596
10	0.75	18.3 (126)	24.1 (166)	21.4 (147)	28.2 (194)	0.204	0.595	−0.558	1.000	1.149
2	1.0	23.1 (159)	22.8 (157)	28.6 (197)	28.2 (195)	0.261	0.768	−0.736	0.959	1.135
1	1.5	27.2 (187)	18.2 (126)	36.9 (254)	24.7 (170)	0.345	0.960	−0.952	0.777	0.876
3	1.99	32.0 (221)	16.0 (110)	42.5 (293)	21.2 (146)	0.409	0.740	−0.707	0.533	0.619
5	3.0	34.9 (241)	11.2 (77.2)	46.7 (322)	15.0 (104)	0.486	0.441	−0.408	0.385	0.503
7	4.16	39.8 (275)	9.6 (66.2)	53.2 (367)	12.8 (88.2)	0.520	0.290	−0.265	0.367	0.556
9	PS	45.0 (310)	0	57.6 (397)	0	0.577	0	0	0.315	0.450
14	2.0 ($\Sigma \to \mathcal{T}$)	32.1 (221)	16.9 (116)	44.4 (306)	23.4 (161)	0.397	0.780	−0.750	0.650	0.797
17	2.0 ($\mathcal{T} \to \Sigma$)	34.7 (239)	16.0 (110)	48.7 (336)	22.5 (155)	0.424	0.682	−0.646	0.493	0.593
12	1.0 ($\Sigma \to \mathcal{T}$)	23.1 (159)	21.7 (150)	28.5 (197)	26.9 (185)	0.270	0.798	−0.769	0.829	1.182
13	1.0 ($\mathcal{T} \to \Sigma$)	22.9 (158)	22.7 (157)	29.3 (202)	29.1 (200)	0.260	0.765	−0.733	0.824	0.948

[a] Under pure torque deformation did not localize and no failure was observed.

increase with α. With the notable exception of the pure torsion results, each of the other responses exhibit a limit load marked with the symbol ◆ ($(\Sigma_{\max}, \mathcal{T}_{\max})$ and $(\varepsilon_{22L}, \varepsilon_{12L})$ listed in Table 1). It is followed by a descending part during which the deformation localizes. The strain paths in Fig. 9b follow nearly linear trajectories with a significant portion of the growth coming after the limit load. The equivalent strain-rotation plot in Fig. 11 shows a similar trend in that each trajectory takes a significant upturn after the limit load. The highest strain values plotted come from the last image recorded before the onset of failure. The nominal and true stresses as well as the *Mean* and *Max* equivalent strains at failure are listed Table 2.

In five of the experiments with lower values of α, deformation localized in the middle of test section and the ensuing fracture

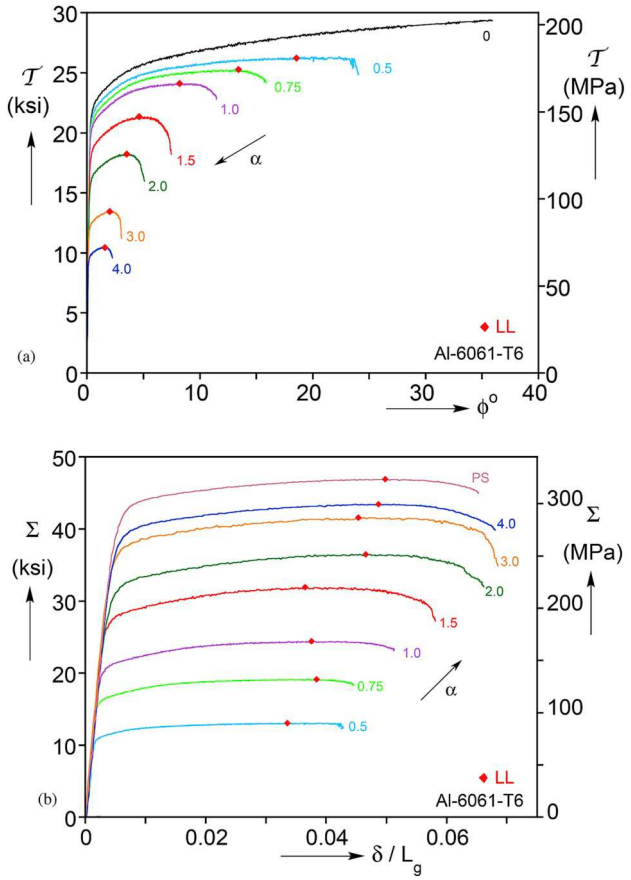

Fig. 10. (a) Nominal shear stress-rotation responses for the full set of radial path experiments. (b) Nominal axial stress-normalized elongation responses.

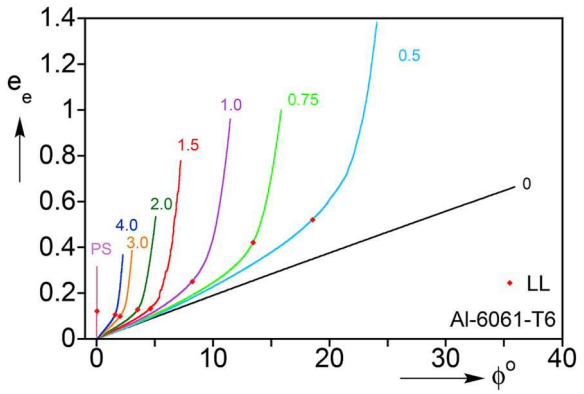

Fig. 11. *Mean* equivalent plastic strain vs. rotation for full set of radial path experiments.

followed the trough of the localization. For the two higher values of α (3.0 and 4.0), localization occurred closer to the edge of the test section presumably due to the stress concentration caused by the circular fillet. In the plane strain experiment, localized deformation meandered between the lower edge and the center of the test section. Closer to failure the deformation grew preferentially in one area of this serpentine band.

The fracture surfaces exhibited the usual dimples, indicative of the void growth and coalescence mechanisms typical of ductile failure. However, as reported in Ghahremaninezhed and Ravi-Chandar (2012, 2013) and Haltom et al. (2013), we expect that this effect was local to the failure surface. Furthermore, X-ray tomography performed on a similar specimen of the same alloy revealed very small porosity in the immediate vicinity of the failure zone (see Section 4 Scales et al. (2016)). Roth et al. (2018) used X-ray tomography to monitor the evolution of voids during biaxial tests on dual-phase steel, and reported significant void growth as failure

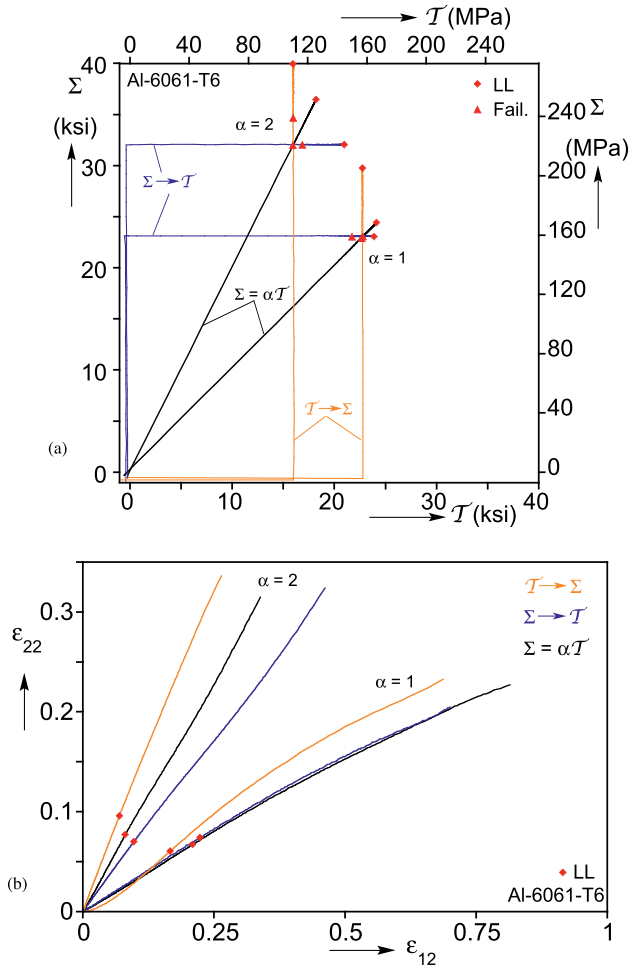

Fig. 12. (a) Nominal axial-shear stress paths for the two sets of radial and corner path experiments with $\alpha = 1.0$ and $\alpha = 2$. The limit load is marked by ◆ and failure by ▲. (b) Corresponding *Mean* strain histories.

was approached. This indicates that the evolution of damage is strongly material dependent.

The results for the pure torsion test included in the figures ($\alpha = 0$) differ from the rest in several ways. First the simple shear stress recorded remains monotonically increasing up to an equivalent strain of 0.6 when the test was terminated because the section showed first signs of buckling. Consequently, the circumferential band of localized deformation observed for all other tension-torsion experiments in the set did not develop, and this is responsible for the linear $e_e - \phi$ response in Fig. 11. Probably for the same reason the specimen did not rupture in any way. It is also interesting to observe that, as is evident in Fig. 9b, the test section elongated by a small amount as reported by Swift (1947).

3.3. Corner loading paths

The path-dependence of failure was explored through two additional pairs of experiments in which loading followed corner paths. The stress histories are shown in Fig. 12a. The pairs correspond to the radial path experiments with $\alpha = 1.0$ and 2.0. They consist of an experiment in which the specimen is preloaded in tension and then loaded to failure in shear ($\Sigma \rightarrow \mathcal{T}$), and a second one in which it is preloaded in shear and then loaded to failure in tension. For the ($\Sigma \rightarrow \mathcal{T}$) paths, the specimen is first loaded axially in displacement control up to the nominal axial stress at which failure occurred in the corresponding radial path experiment. When the specified load is reached, it is maintained by switching the controller into load control. The specimen is then subjected to torsional loading under rotation control until failure. In the case of the ($\mathcal{T} \rightarrow \Sigma$) paths the order is reversed: The specimen is first torqued until the nominal shear stress reaches the value at which failure occurred in the corresponding radial path experiment, and from then on the specimen is loaded axially to failure under displacement control while the torque is maintained.

The recorded shear stress-rotation and axial stress-elongation responses recorded for the three $\alpha = 2.0$ experiments are compared in Fig. 13 and those for the $\alpha = 1.0$ experiments in Fig. 14. The axial-shear strain trajectories traced for each of the three paths for both values of α are compared in Fig. 12b. The geometric parameters and the stresses and strains of interest for the corner

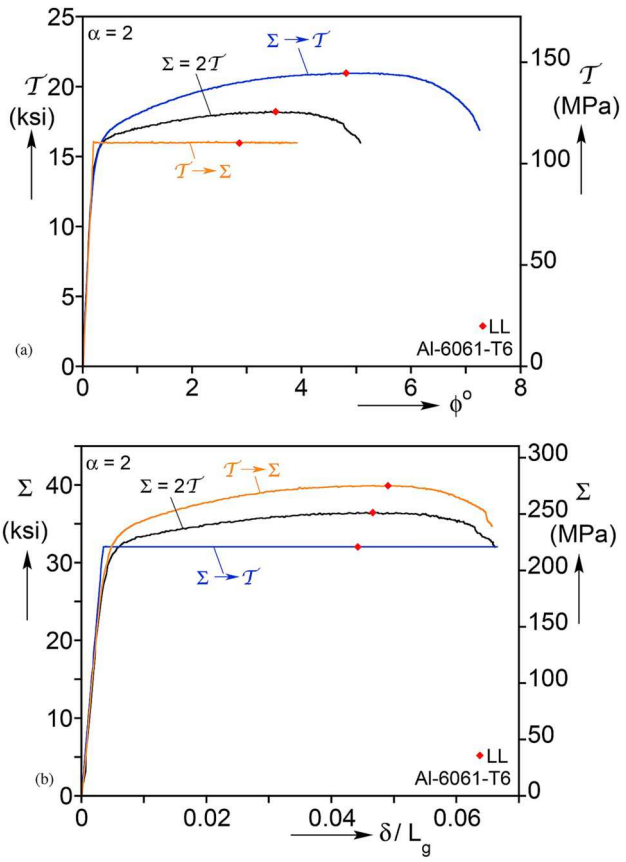

Fig. 13. (a) Nominal shear stress-rotation responses for the set of radial and corner path experiments with $\alpha = 1$. (b) Nominal axial stress-normalized elongation responses.

experiments are included in Tables 1 and 2.

In the two $\alpha = 2.0$ corner-path experiments, deformation remains elastic during the preloading phase. For both paths the stress in the second branch following the corner traces a higher trajectory than in the corresponding radial path. Thus for the $(\Sigma \rightarrow \mathscr{T})$ path $\mathscr{T}_{max}$= 21 ksi (145 MPa) and for the radial path 18.2 ksi (126 MPa); and for $(\mathscr{T} \rightarrow \Sigma)$ Σ_{max}= 39.9 ksi (275 MPa) vs. 36.5 ksi (252 MPa) for the radial path. Interestingly, despite these differences, the nominal stresses at failure are still very close to the values at which the radial path failed (see values in Table 2 and proximity of the failure points in Fig. 12a). The true stress at failure listed in Table 2 differ somewhat more between the three paths apparently because of differences in the final strains.

As expected, the strains plotted in Fig. 12b, follow nearly linear but different trajectories for the three paths. The differences in these paths, however, are in concert with the difference in stress levels seen in Fig. 13. For example, the $(\Sigma \rightarrow \mathscr{T})$ experiment for $\alpha = 2.0$ reached greater level of shear stress than its radial counterpart, and consequently its strain history exhibits more shear deformation. The same holds for the $(\mathscr{T} \rightarrow \Sigma)$ experiment, which traces greater axial stresses than the radial path experiment and exhibits a more axially-dominant strain trajectory. The strains at the load maxima are of the same order and for all paths most of the deformation takes place after the load maximum. The equivalent strains at failure for the radial and two corner paths listed in Table 2 have values that are comparable.

The $\alpha = 1.0$ experiments exhibit similar trends with the following differences. In the $(\mathscr{T} \rightarrow \Sigma)$ path the test section underwent some plastic deformation during the initial shearing and the subsequent axial stress branch reached a value that is 22% higher than Σ_{max} achieved in the radial path. Despite this, the axial stresses at failure are again essentially identical. The $(\Sigma \rightarrow \mathscr{T})$ experiment traced essentially the same level of shear stress as its radial path counterpart, and accordingly their strain trajectories follow very similar paths. The equivalent strains at failure are around 1.1.

4. Discussion of failure

The measured *Max* and *Mean* equivalent strains, e_{ef}^{p} and $\bar{e}_{ef}^{p}$, in the last image prior to failure in each experiment are plotted against the measured triaxiality, σ_{mf}/σ_{ef}, in Fig. 15a using the von Mises measures of stress and strain. The numerical values are also listed in Table 2 together with the corresponding Lode parameters $\bar{\theta}_f$ and μ_f (see Eqs. (8) and (9)). The two failure strain measures follow similar, monotonically decreasing trends as the triaxiality increases, with the *Max* values being consistently higher than the *Mean*.

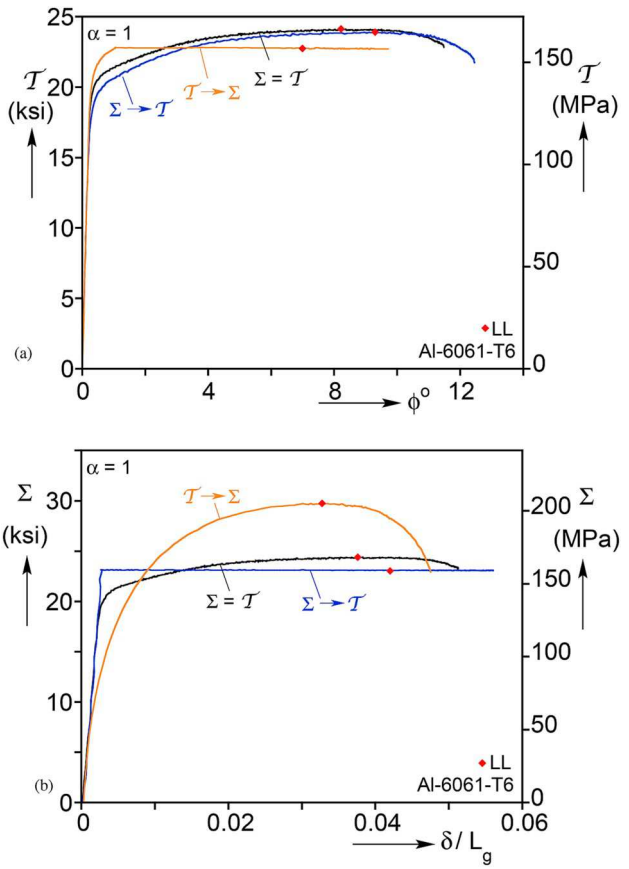

Fig. 14. (a) Nominal shear stress-rotation responses for the set of radial and corner path experiments with $\alpha = 2$. (b) Nominal axial stress-normalized elongation responses.

The maximum value of strain recorded was 1.596 at a triaxiality of 0.139 ($\alpha = 0.5$), while for the highest triaxiality experiment was 0.450 (plane-strain tension experiment). For the range of triaxiality values considered ($0 \leq \sigma_{mf}/\sigma_{ef} \leq 0.577$), the monotonic trends with triaxiality and the levels of the failure strains are in line with the values reported in Scales et al. (2016). The strain levels are again significantly larger than other published results for this alloy, presumably because they originate from within a localized zone that develops largely free of constraints. Furthermore, the trend does not exhibit a cusp in the vicinity of triaxiality of 0.33 reported in some investigations. Recall that the *Mean* values are calculated from all column maxima. Therefore the values reported have corresponding standard deviations. Six of the experiments had standard deviations of less than 0.07, while in the shear-dominant $\alpha = 0.5$ experiment it was 0.11 (see Chapter 4 in Scales, 2018).

The Lode parameter $\mu(\alpha)$ is plotted against triaxiality over the stress states of the experiments ($0 \leq \sigma_m/\sigma_e \leq 0.577$) in Fig. 15b. This parameter takes a value of 0 for simple shear, decreases down to -1.0 at triaxiality of about 0.33, and returns to 0 for plane strain tension test. Included in the figure with solid bullets are the values of μ at failure in the experiments (see Table 2).

Fig. 15a also shows the *Mean* measures of failure strain for the ($\mathcal{T} \rightarrow \Sigma$) and ($\Sigma \rightarrow \mathcal{T}$) corner paths corresponding to the radial paths with $\alpha = 1.0$ and 2.0. The corner path failure strains are generally comparable to their radial path counterparts. The corresponding differences between the *Max* measures of failure strain in Table 2 are somewhat larger but this could be caused by the larger scatter exhibited by the *Max* data. It's worth mentioning that this level of agreement in failure strains between corner and radial path experiments was also reported in Haltom (2012).

In order to include the effect of the material frame rotation resulting from shear deformations, all strains reported here were integrated over the history of the test (see Section 2.3). By contrast, Haltom et al. (2013) and Scales et al. (2016), motivated by the desire to report strains free of the influence of a constitutive model, reported the total strains measured just before the onset of failure. To assess the influence of material frame rotation on the results, the reported *Max* and *Mean* failure strains are compared to the total measures in Fig. 16. As expected, the difference between the two measures is very small for the tension-dominant larger values of α, become noticeable for α of 1.0 and 0.75 while for the shear-dominant case of $\alpha = 0.5$ the *Mean* and *Max* total measures are respectively 14.5% and 11% lower than the integrated measure.

The integration of the strains invariably requires the adoption of a constitutive model through Eq. (11). The analysis of the tension-torsion experiments in Part II uses the isotropic non-quadratic Hosford yield function and the anisotropic Barlat et al. (2005) yield functions, in addition to von Mises. Adopting these constitutive models introduces a different definition of σ_e and alters σ_m as the

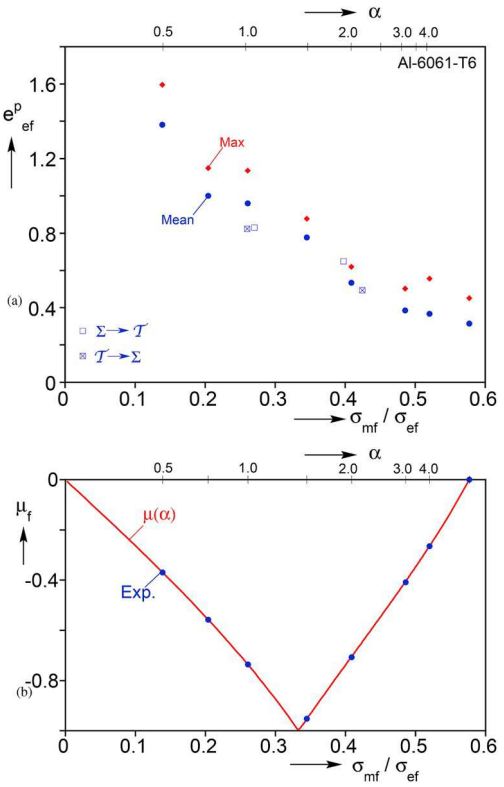

Fig. 15. (a) Measured *Mean* and *Max* equivalent strains at failure plotted against the measured triaxiality, assuming a von Mises constitutive model. (b) Variation of the Lode parameter over the same range of triaxiality.

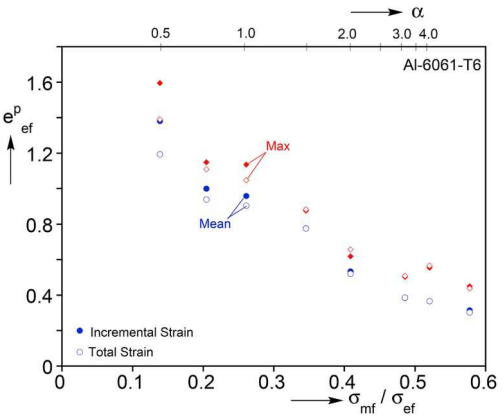

Fig. 16. (a) Measured *Mean* and *Max* equivalent strains at failure vs. triaxiality, calculated incrementally (●, ◆), and also in the "total" manner used in Haltom et al. (2013) and Scales et al. (2016) (○, ◊).

constant of proportionality β between the axial and hoop stress in (2a) depends on the adopted constitutive model. The effect of the constitutive model on the *Mean* measure of failure strain is demonstrated in Fig. 17 where it is plotted against the triaxiality, with the variables based on the von Mises (VM), Hosford (H8), and Yld04-3D models. Note that σ_e used in triaxiality is the one corresponding to each constitutive model. The values of β used in the calculation of σ_e and σ_m for VM, H8 and Yld04-3D appear in Fig. C1, where they are plotted against the stress ratio α. The difference between the three failure strains is small across the whole range of triaxiality. The effect on the value of the triaxiality is more noticeable as it results in a horizontal spread between the data points of each experiment. The horizontal shift is more significant for the larger values of triaxiality, where for example for $\alpha = 4.16$, σ_m/σ_e drops from 0.520 for VM to 0.452 for H8, with the Yld04-3D value in between the two. In summary, since the effect of the constitutive model on the failure strain is quite small, and the shifts in triaxiality are modest, the monotonic decreasing trend of the failure strains with triaxiality, and the high level of failure strains are maintained for all three constitutive models considered.

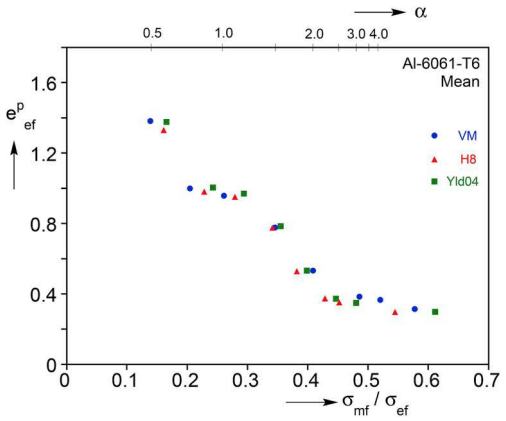

Fig. 17. *Mean* failure strains vs. triaxiality, calculated incrementally with three different constitutive models: von Mises (VM), Hosford with exponent 8 (H8), and Barlat (Yld04).

5. Summary and conclusions

This investigation deals with the ductile failure of metals under moderate and low triaxiality values, which has challenged researchers during the last decade. The aim of the present study is to use careful experiments and complementary analysis to add clarity to the problem. Part I of two sister papers presented the results of a new set of tension-torsion experiments on Al-6061-T6 tubes tested under proportional and non-proportional stress histories. The specimens have a test section that is thin enough for the through thickness stress to be negligible, and long enough to allow the localization that precedes failure to develop unimpeded. Furthermore, the test section is free of edge effects that complicate the onset of failure in other test specimen designs. The paper also includes results from a set of tension-pressure biaxial experiments that are used in conjunction with the tension-torsion responses in the calibration of the Yld04-3D anisotropic yield function in Part II. The shear dominant experiments take the material to rather large strains. Simulation of these experiments requires material hardening that extends much further than the strain provided from a tensile test. Therefore the hardening of the material was extracted from a pure torsion test instead. The measured simple shear response is used in Part II to extract the material hardening.

In both the radial and corner path experiments the test section remained nearly uniform deeply into the plastic regime. They all eventually developed nominal stress maxima, which were followed by localized deformation in narrow circumferential zones with widths of the order of the wall thickness. The high resolution 3-D DIC used enabled continuous monitoring of the deformation both during the uniform and localized phases. Deformation in the necked zones grew nearly exponentially and developed sharp gradients, reaching strain levels hitherto unmatched by other experimental programs. Rupture eventually occurred typically in the deepest part of the neck. The failure strains reported were extracted from the last DIC image of the necked zone just prior to rupture in the neighborhood of the crack that forms. Thus the value reported can be considered to be a lower bound. The reported stresses at failure are based on the assumptions that the test section remains uniform, its radius does not change, and through thickness stress are negligible. These assumptions are violated to some degree particularly so inside the neck. The following conclusions on failure are drawn from this study.

- The high failure strain levels and monotonic decrease with triaxiality follow and confirm the trend of the results in Scales et al. (2016) for the same alloy.
- Integration of the strains over the path results in failure strains that are very close to the final values measured directly from the last recorded DIC image for most of the stress states covered. For triaxialities below 0.2 a measurable difference was recorded with the integrated values being somewhat larger. This difference does not change the monotonicity of the failure strains.
- Integration of the strains requires the adoption of a constitutive model. The integrated equivalent plastic strain at failure is not significantly affected by the three constitutive models we considered. The difference in the failure strain among the three

constitutive models is well within the measurement error.

- Adoption of different constitutive models introduces a new definition of triaxiality through the associated equivalent stress and the change in mean stress through the parameter β in Eq. (3). The resultant changes are minor for low values triaxialities, somewhat larger for higher values but they do not change the monotonic nature of the failure-triaxiality locus.
- Despite the significant changes in the stress introduced by the four corner paths considered, and the resultant differences in the stress levels at the limit loads, the state of stress and equivalent strain at failure were found to be close to the values of corresponding radial paths. This suggests a relative insensitivity of the failure strain on stress path at least in the stress regime examined.

Acknowledgments

The authors acknowledge with thanks financial support for this work received from the National Science Foundation through the GOALI grant CMMI-1663269. We also thank Dr. Raja K. Mishra of General Motors for cooperation and technical interactions. Special thanks go to Robert Kubic of GM for conducting the EBSD scans and his insight on microstructures.

Appendix A. Response of Al-6061-T6 Tubes Under Combined Internal Pressure and Axial Force

The analysis of the tension-torsion experiments in Part II incorporates the Yld04-3D anisotropic yield function (Barlat et al., 2005). Calibration of the 18 anisotropy parameters of this constitutive model requires a broader set of stress states than those available from the tension-shear results presented in Part I. Thus the calibration data were enriched with a set of axial-hoop stress states that are outlined here.

The additional biaxial stress-states were generated through a set of internal pressure-axial load experiments performed on the same 2-inch (50 mm) diameter tubular stock as that of the tension-torsion specimens. A 4 in (102 mm) test section with a 0.050 in (1.27 mm) wall thickness was machined into a 12 in (305 mm) long test specimen. It was mounted in the biaxial set-up shown schematically in Fig. A1. Axial force is applied by a 50 kip (222 kN) servo-hydraulic testing machine and internal pressure by an independent hydraulic closed-control pressurizing system (capacity 10,000 psi—690 bar). Tubes were loaded under radial paths in the hoop-axial stress space, i.e.,

$$\Sigma = \eta \Sigma_\theta \, (\eta = \text{ cont.}), \tag{A1}$$

where Σ and Σ_θ are respectively the nominal axial and hoop stresses. The nominal stresses are calculated from the applied pressure (P) and axial force (F) via:

$$\Sigma_\theta = \frac{PR}{t}, \;\; \Sigma = \frac{F}{2\pi Rt} + \frac{PR}{2t}, \tag{A2}$$

where R is the radius of the test section and t its initial wall thickness. The experiments were conducted with the pressurizing system in volume control and the induced pressure acting as a command signal for the axial force, thus achieving the required relationship between pressure and force (see similar experiments in Korkolis and Kyriakides (2008); Korkolis et al. (2010)). The deformation in the test section was continuously monitored by the DIC system as outlined in Section 2.1, but here the cameras were oriented vertically and further apart to accommodate the long, cylindrical test section. For the loadings of interest here, the test section deformation remained uniform so a relatively large facet size and spacing of about $1.2t$ and $0.4t$ were found to suffice.

Eight experiments were conducted with biaxiality ratios:

$$\eta = \{0, 0.25, 0.5, 0.62, 0.75, 0.9, 1.0, 1.2\}.$$

The linear stress paths traced are plotted in Fig. A2a and the corresponding strains in Fig. A2b. Included in the two figures are the stress and strain paths from a uniaxial tension test performed on an axial strip extracted from a tube. Figures A3a and A3b show respectively the hoop stress-strain ($\Sigma_\theta - \varepsilon_{11}$) and axial stress-strain ($\Sigma - \varepsilon_{22}$) responses. Marked on these with a symbol ▲ is the location of plastic work of 1000 psi (6.897 MPa) at which data were collected for the calibration of Yld04-3D. (More details about these experiments are reported in Scales (2018)).

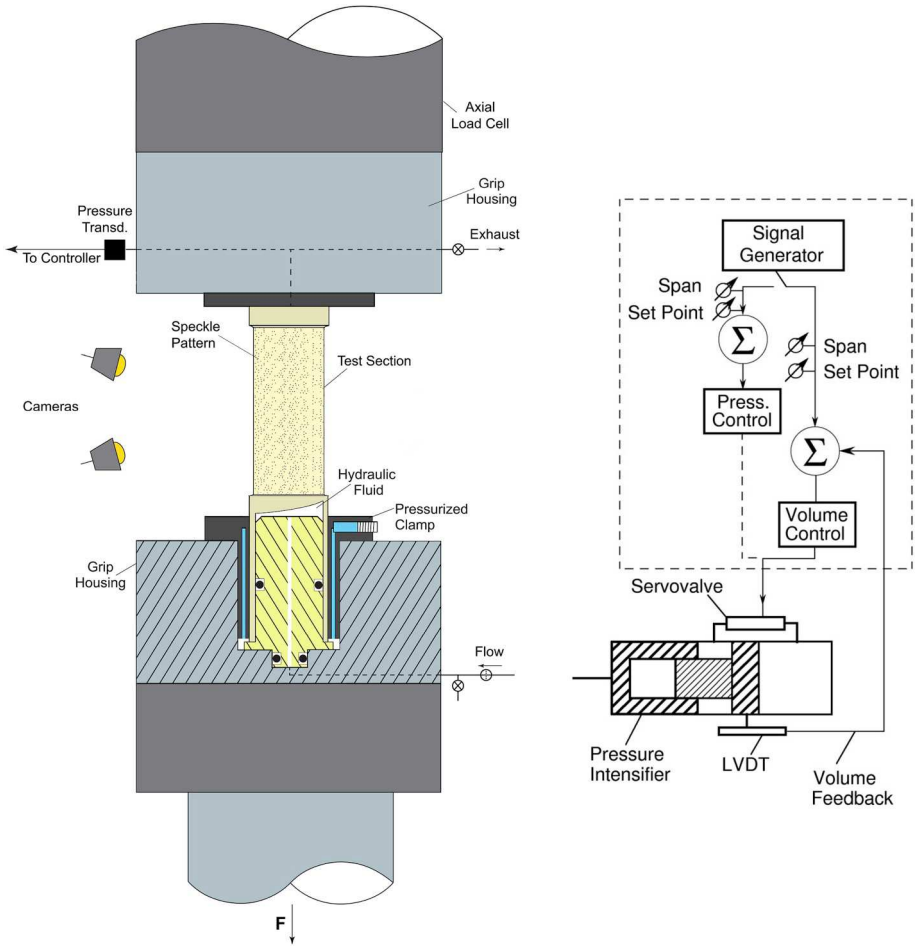

Fig. A1. Schematic of the internal pressure-tension experimental setup. Included on the right is the closed loop pressurization system.

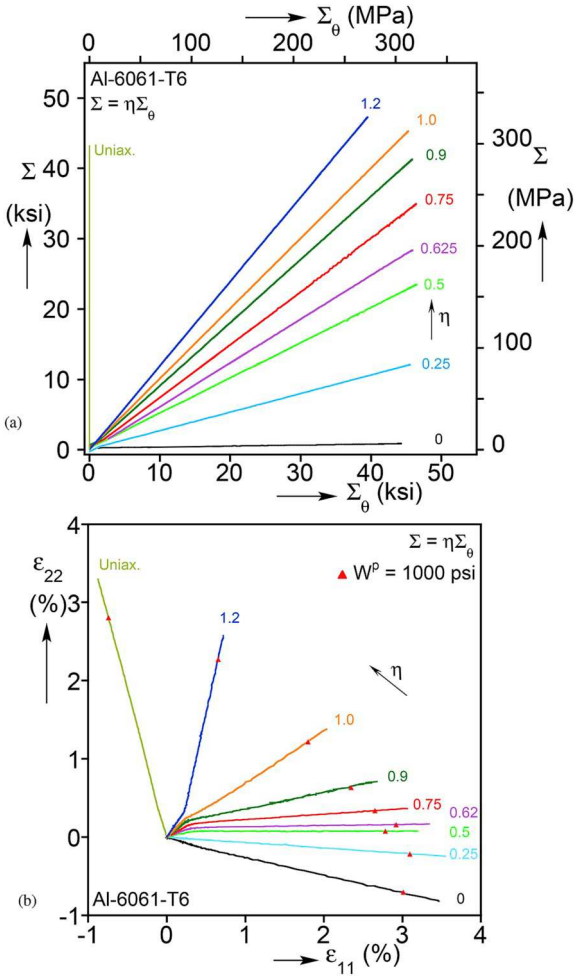

Fig. A2. (a) Prescribed nominal stress histories of the eight pressure-tension tests. Included is a the response from a uniaxial tension test–"Uniax." (b) Corresponding strain histories.

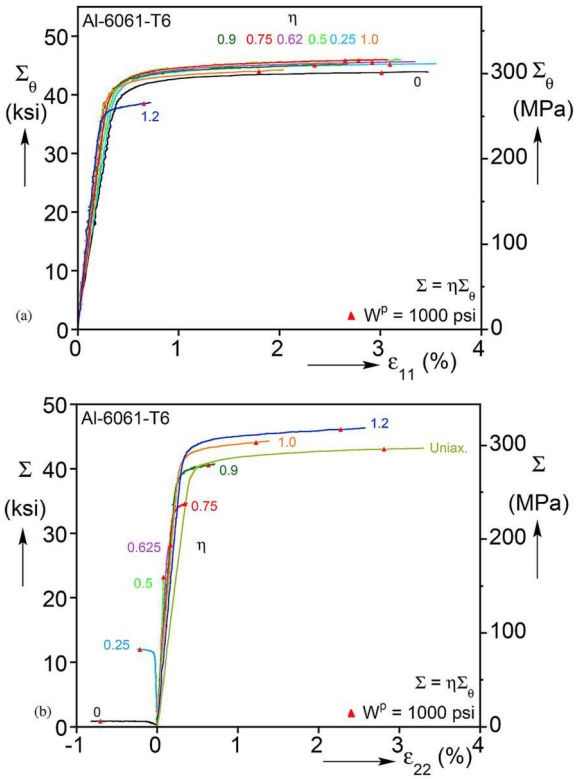

Fig. A3. (a) Nominal hoop stress and strain responses of the eight pressure-tension experiments. (b) Axial stress-strain responses.

Appendix B. Grain Morphology

Aluminum 6061-T6 is a precipitation-hardened alloy with the following chemical composition.

Table B1
Al-6061-T6 chemical composition

Si	Fe	Cu	Mn	Mg	Cr	Zn	Ti
0.59	0.26	0.23	0.05	0.99	0.10	0.05	0.02

The current tension-torsion test specimens had a yield stress of 40.8 ksi (281 MPa) compared to 43.2 ksi (298 MPa) for those in Scales et al. (2016), and exhibited very similar hardening and, by and large, similar ductility.

The undeformed grain morphology was assessed via Electron Back Scattering Diffraction (EBSD) analysis. The two scans discussed below were conducted on material extracted from an undeformed test specimen. Results from a scan in the $\theta - x$ plane over an area of approximately 4×4 mm are presented in Fig. B1. The images were processed in ImageJ and ellipses were fit to 540 grains. Distributions of the major and minor ellipse diameters ($2a$ and $2b$) are presented in Fig. B2. The mean major and minor diameters are 148 and 88 μm and have standard deviations of 80 and 51 μm respectively.

A through-thickness scan (r-x plane) of a specimen is presented in Fig. B1b. The scan is roughly 7 mm in length and covers the entire wall-thickness. Note however that due to edge effects some of the material along the OD and ID were missed, and therefore the image shown is only 0.031 in (0.79 mm) wide, in contrast to the nominal wall thickness of 0.0385 in (0.97 mm). It is readily apparent from this scan that two distinct grain-size regimes exist: the grains along the ID are elongated and larger than those along the OD. Recall that the ID surface of the test specimens *are not* machined and are therefore the original extrusion surface. A statistical analysis like the one described above for the through-thickness scan shows mean major and minor diameters of 178 and 60 μm. The grains on the outer edge on the RHS are longer and narrower in the $r - x$ plane than the grains in internal surface of the $\theta - x$ plane of the specimen. Such through-thickness variations in grain size have been observed in other extruded products (e.g., Khadyko et al. (2016)) but their effect on the mechanical behavior of the material remains unclear.

It is also worth reporting that these grains are larger than what was found in the materials tested in Haltom et al. (2013) and Scales et al. (2016), which had average major and minor diameters of 33 μm and 20 μm (see Fig. 16 in the first reference). Despite this difference, the yield stress and hardening for these two sets of material were similar. This indicates that precipitates play a larger role than the grain size distribution.

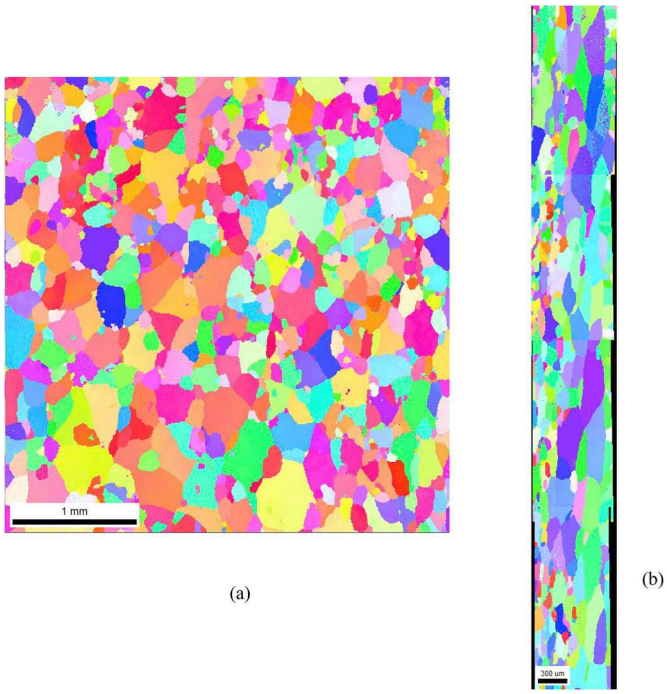

Fig. B1. (a) EBSD scan of undeformed material extracted from a machined but untested specimen ($\theta - x$ plane). (b) EBSD scan through the test section wall thickness (r-x plane).

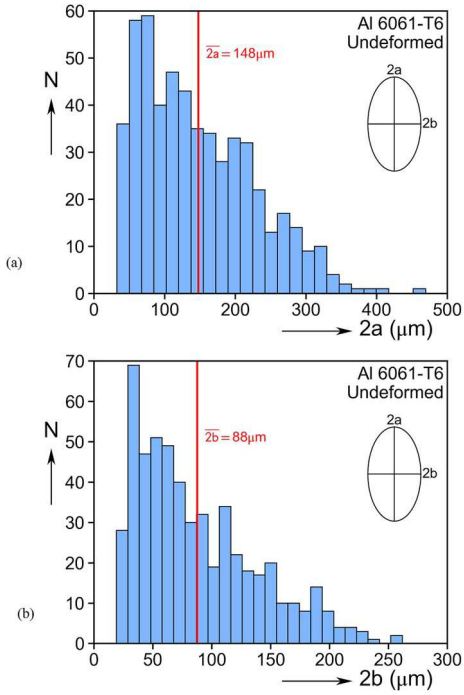

Fig. B2. (a) Distribution of major axes of ellipses fit to the grains in Fig. B1(a), and (b) distribution of minor axes.

Appendix C. Value of β

For the purposes of calculating the equivalent plastic strain increment and the triaxiality at failure for the vM, H8 and Yld04-3D constitutive models, the hoop strain ε_{11} was assumed to be negligibly small. Based on this assumption $\sigma_{11} = \beta\sigma_{22}$ where β depends on the stress ratio α as shown in Fig. C1.

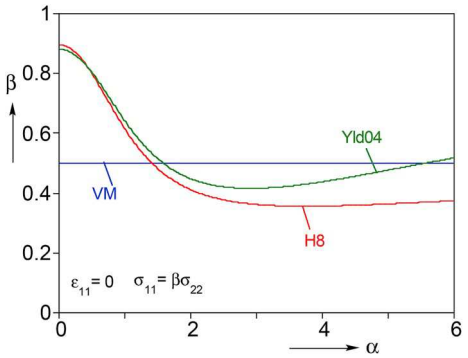

Fig. C1. Evolution of the parameter β with the stress ratio α for the three constitutive models considered.

References

Abi-Akl, R., Mohr, D., 2017. Paint-bake effect on the plasticity and fracture of pre-strained aluminum 6451 sheets. Int. J. Mech. Sci. 124/125, 68–82.

Bao, Y.-B., Wierzbicki, T., 2004. On fracture locus in the equivalent strain and stress triaxiality space. Int. J. Mech. Science 46, 81–98.

Bai, Y.-L., Wierzbicki, T., 2008. A new model of metal plasticity and fracture with pressure and Lode dependence. Int. J. Plasticity 24, 1071–1096.

Bai, Y.-L., Wierzbicki, T., 2010. Application of extended Mohr-Coulomb criterion to ductile fracture. Int. J. Fracture 161, 1–20.

Barlat, F., Aretz, H., Yoon, J.W., Karabin, M.E., Brem, J.C., Dick, R.E., 2005. Linear transformation-based anisotropic yield functions. Int. J. Plasticity 21, 1009–1039.

Barsoum, I., Faleskog, J., 2007. Rupture mechanisms in combined tension and shear–Experiments. Int. J. Solids Struct. 44, 1768–1786.

Beese, A.,M., Luo, M., Li, Y., Bai, Y., Wierzbicki, T., 2010. Partially coupled anisotropic fracture model for aluminum sheets. Eng. Fract. Mech. 77, 1128–1152.

Benzerga, A.A., Leblond, J.-B., 2010. Ductile fracture by void growth to coalescence. Adv. Appl. Mech. 44, 169–305.

Faleskog, J., Barsoum, I., 2013. Tension-torsion fracture experiments-Part I: experiments and a procedure to evaluate the equivalent plastic strain. Int. J. Solids Struct. 50, 4241–4257.

Ghahremaninezhad, A., Ravi-Chandar, K., 2012. Ductile failure behavior of polycrystalline Al 6061-T6. Int. J. Fracture 174, 177–202.

Ghahremaninezhad, A., Ravi-Chandar, K., 2013. Ductile behavior in polycrystalline aluminum alloy Al 6061-T6 under shear dominant loading. Int. J. Fract. 180, 23–39.

Gurson, A., 1977. Continuum theory of ductile rupture by void nucleation and growth: Part I – yield criteria and flow rules for porous ductile media. J. Eng. Mater. Technol. 99, 2–15.

Ha, J., Baral, M., Korkolis, Y.P., 2018. Plastic anisotropy and ductile fracture of bake-hardened AA6013 aluminum sheet. Int. J. Solids Struct. 155, 123–139.

Haltom, S.S., 2012. On the Ductile Failure of Thin-Walled Aluminum Alloy Tubes under Combined Shear and Tension. University of Texas at Austin MS Thesis, Engineering Mechanics.

Haltom, S.S., Kyriakides, S., Ravi-Chandar, K., 2013. Ductile failure under combined shear and tension. Int. J. Solids Struct. 50, 1507–1522 2013.

Hosford, W.F., 1972. A generalized isotropic yield criterion. ASME J. Appl. Mech. 39, 607–609.

Johnson, G.R., Cook, W.H., 1985. Fracture characteristics of three metals subjected to various strains, strain rates, temperatures and pressures. Eng. Fract. Mech. 21, 31–48.

Khadyko, M., Dumoulin, S., Hopperstad, O.S., 2016. Texture gradients and strain localization in extruded aluminium profile. Int. J. Solids Struct. 9**7–98**, 239–255.

Korkolis, Y.P., Kyriakides, S., 2008. Inflation and burst of anisotropic tubes for hydroforming applications. Int. J. Plasticity 24, 509–543.

Korkolis, Y.P., Kyriakides, S., Giagmouris, T., Lee, L.-H., 2010. Constitutive modeling and rupture predictions of Al-6061-T6 tubes under biaxial loading paths. ASME J. Appl. Mech. 77 (5), 1–5 064501.

McClintock, F.A., 1968. A criterion for ductile fracture by growth of holes. ASME J. Appl. Mech. 35, 363–371.

McClintock, F.A., 1971. Plasticity aspects of fracture. In: In: Liebowitz, H. (Ed.), Fracture an Advanced Treatise, vol. III. pp. 48–220.

Papasidero, J., Doquet, V., Mohr, D., 2015. Ductile fracture of aluminum 2014-T351 under proportional and non-proportional multi-axial loading: Bao-Wierzbicki results revisited. Int. J. Solids Struct. 69–70, 459–474.

Rice, J.R., Tracey, D.M., 1969. On the ductile enlargement of voids in triaxial stress fields. J. Mech. Phys. Solids 17, 201–217.

Roth, C., Morgeneyer, T., Cheng, Y., Helfen, L., Mohr, D., 2018. Ductile damage mechanism under shear-dominated loading: in-situ tomography experiments on dual phase steel and localization analysis. Int. J. Plast. 109, 169–192.

Scales, M., 2018. Localization and Failure of Aluminum 6061-T6 under Biaxial Loading. University of Texas at Austin Ph.D. Dissertation, Engineering Mechanics.

Scales, M., Tardif, N., Kyriakides, S., 2016. Ductile failure of aluminum alloy tubes under combined torsion and tension. Int. J. Solids Struct. 97–98, 116–128.

Swift, H.W., 1947. Length changes in metals under torsional overstrain. Engineering 163, 253–257.

Tvergaard, V., 1990. Material failure by void growth to coalescence. Adv. Appl. Mech. 27, 83–151.